Bulletin of the Seismological Society of America, Vol. 104, No. 5, pp. 2529–2540, October 2014, doi: 10.1785/0120140047

Relation of Landslides Triggered by the Kiholo Bay Earthquake to Modeled Ground Motion

by Edwin L. Harp, Stephen H. Hartzell, Randall W. Jibson, Leonardo Ramirez-Guzman, and Robert G. Schmitt

Abstract The 2006 Kiholo Bay, Hawaii, earthquake triggered high concentrations of rock falls and slides in the steep canyons of the Kohala Mountains along the north coast of Hawaii. Within these mountains and canyons a complex distribution of landslides was triggered by the earthquake shaking. In parts of the area, landslides were preferentially located on east-facing slopes, whereas in other parts of the canyons no systematic pattern prevailed with respect to slope aspect or vertical position on the slopes. The geology within the canyons is homogeneous, so we hypothesize that the variable landslide distribution is the result of localized variation in ground shaking; therefore, we used a state-of-the-art, high-resolution ground-motion simulation model to see if it could reproduce the landslide-distribution patterns. We used a 3D finite-element analysis to model earthquake shaking using a 10 m digital elevation model and slip on a finite-fault model constructed from teleseismic records of the mainshock. Ground velocity time histories were calculated up to a frequency of 5 Hz. Dynamic shear strain also was calculated and compared with the landslide distribution. Results were mixed for the velocity simulations, with some areas showing correlation of landslide locations with peak modeled ground motions but many other areas showing no such correlation. Results were much improved for the comparison with dynamic shear strain. This suggests that (1) rock falls and slides are possibly triggered by higher frequency ground motions (velocities) than those in our simulations, (2) the ground-motion velocity model needs more refinement, or (3) dynamic shear strain may be a more fundamental measurement of the decoupling process of slope materials during seismic shaking.

Introduction

Many studies of seismically triggered landslides have noted a correlation between the distribution of triggered landslides and prominent topographic features such as steep ridges and promontories on the ends of ridges (Harp *et al.*, 1981; Çelebi, 1986; Harp and Jibson, 1995, 1996, 2002; Meunier *et al.*, 2008) above and beyond the normal correlation with steep slopes alone. Amplification of shaking by steep topography is commonly invoked as the cause for this nonrandom distribution of triggered landslides, but direct evidence for this—other than the landslide distribution itself—generally is lacking. Although field studies have observed and measured topographic amplification of ground shaking (e.g., Çelebi, 1986; Hartzell *et al.*, 1994, 2014), no study has directly compared a specific landslide distribution to topographically amplified ground shaking. Our intent in this paper is to do just that—to model the topographic effects of propagating seismic waves and to compare the predicted shaking to the locations of landslides triggered by the 2006 Kiholo Bay, Hawaii, earthquake.

Some previous studies have provided qualitative evidence that topographic amplification affects the distribution of landsliding. Meunier *et al.* (2007) documented the 2D (cross sectional) spatial distribution of seismically triggered landslides with respect to the fault and topography for three earthquakes and concluded that topographic amplification caused landslides to preferentially occur near ridge crests. Harp and Jibson (2002) showed that, in multiple earthquakes, anomalously high concentrations of landslides in Pacoima Canyon, California, were most likely caused by topographic amplification. Sepulveda *et al.* (2005) studied the same area by modeling slope stability in amplified and nonamplified conditions and showed that topographic amplification was necessary to produce the landslides triggered by the 1994 Northridge earthquake. Other studies have more broadly related landslide distributions to regional models of ground-motion distribution. Harp and Wilson (1995) and Jibson and Harp (2012) compared the spatial limits of triggered landslides to strong-motion levels using recorded and interpolated

ground shaking. Comparison of the distribution of strong shaking from an earthquake with the landslide distribution has been conducted using simple comparisons (Khazai and Sitar, 2003; Wang *et al.*, 2010; Dai *et al.*, 2011), statistical regression models (Lee *et al.*, 2008; Lin and Tung, 2003), and deterministic models (Jibson *et al.*, 2000). These studies used existing strong-motion networks to produce interpolated maps of the regional variation of shaking. In summary, previous studies have established threshold shaking limits for landslides and that landslide distributions commonly relate directly to variations in seismic shaking.

Abundant theoretical and observational evidence has shown that topographic features can strongly affect ground motion (Bouchon, 1973; Bard, 1982; Çelebi, 1986; Geli *et al.*, 1988; Ma *et al.*, 2007; Lee *et al.*, 2009; Hartzell *et al.*, 2014). Topographic effects on ground motion are characterized by amplification at mountain or ridge tops and deamplification in valleys for wavelengths close to or slightly less than the width of the topographic feature. The amount of amplification is sensitive to the geometry of the topography with greater amplification associated with sharper features. Steep topography also significantly prolongs ground motion because of the large number of scattered waves. In addition, the amplitude and phase of ground motion may exhibit rapid spatial variation along mountain and ridge slopes, which gives rise to significant differential motions. These characteristics have clear implications for the generation of landslides.

The 2006 Kiholo Bay earthquake triggered an anomalously high concentration of rock falls and rock slides in the Kohala Mountains of Hawaii; in some areas, these landslides were preferentially located on east-facing canyon slopes with few or no failures on corresponding west-facing slopes. In other areas, no such slope preference was observed. This landslide distribution, unlike many others that have exhibited concentrations on ridges and promontories, seemed to be less associated with the tops of ridges and promontories, although the topography of the Kohala Mountains includes extremely narrow ridges and steep canyons. The distribution of these landslides within this canyon topography provided an opportunity to see how closely the pattern of triggered landslides could be replicated by a state-of-the-art ground-motion simulation. Our study uses a fault-slip model (see Data and Resources) constructed from teleseismic records of the mainshock together with a 3D finite-element analysis to predict shaking levels at all cells of a digital elevation model (DEM, see Data and Resources). Cell sizes vary from 20 to 50 m and allow us to investigate the topographic amplification associated with different wavelengths of ground motion and topographic features of different scale. We then compare the modeled shaking to the mapped distribution of landslides.

The Kiholo Bay Earthquake and the Triggered Landslides

The Kiholo Bay, Hawaii, earthquake occurred on 15 October 2006 and had a moment magnitude of 6.7 (see Data and Resources). The focal mechanism solution indicated oblique-normal faulting having a focal depth of approximately 45 km. Instrumentally recorded ground acceleration on Hawaii ranged from 0.05g to 1.12g; the highest recorded motions were to the northeast of the epicenter in the vicinity of the Kohala Mountains (Fig. 1). These high accelerations may be due to impedance contrasts in the velocity profile of the surficial layers in these areas (see Table 1; Wong *et al.*, 2011).

Triggered landslides consisted mainly of widely scattered small-to-moderate size rock falls and rock slides of less than 500 m^3 on road cuts and steep natural slopes on the islands of Hawaii and Maui (Fig. 2). Considerably higher concentrations of rock falls and rock slides occurred in the Kohala Mountains of northern Hawaii (Fig. 3); a few of the largest rock slides in this area had volumes as great as 10,000 m^3 (Fig. 4). Distance limits from the earthquake epicenter to the farthest observed landslides were 56 km to the southeast on Hawaii and 99 km to the northwest on Maui (Fig. 1; Harp and Jibson, 2007). The distribution of landslides outside of the Kohala Mountains was sparse and widely scattered, and no systematic documentation of the complete landslide population was undertaken.

The densely concentrated rock falls and rock slides in the Kohala Mountains occurred within alternating basalt flows and breccias on very steep (60°–80°) slopes. Detailed mapping of these failures indicated a spatial preference of landslide locations on east- to northeast-facing slopes in the northernmost areas of the canyons (Fig. 5a; Harp *et al.*, 2008). Canyons in the northernmost area of the Kohala Mountains along the coast from the Pololu Valley eastward to the Waimanu Valley had a preponderance of falls and slides on east-facing slopes. The smaller canyons in this area along the northern coast show a complete absence of falls and slides on all but east-facing slopes (see Fig. 5a). Elsewhere in the canyons of the Kohala Mountains, the landslide distribution showed little obvious location with respect to slope, elevation, or aspect. Previous landslide scars from any earlier events, either climatic or seismic were not obvious. This is not surprising because the failures from this event were shallow, the slopes subject to daily precipitation, and any similar scars from previous events would likely be undetectable after two or more years.

Ground-Motion Model

To see how closely we could replicate the complicated distribution of landslides within the canyons of the Kohala Mountains, we modeled the ground motion from the Kiholo Bay earthquake using a finite-element code (Tu *et al.*, 2006; Bielak *et al.*, 2010) capable of modeling 3D topographic effects. For the earthquake source model, we used the finite-fault rupture history obtained by Chen Ji (personal communication, 2011) using teleseismic body waves (Fig. 1). The fault plane in this model strikes 86°, dips 42° to the south, and rakes from 180° to 259°. The hypocentral depth is 45 km with rupture primarily to the west from an epicenter

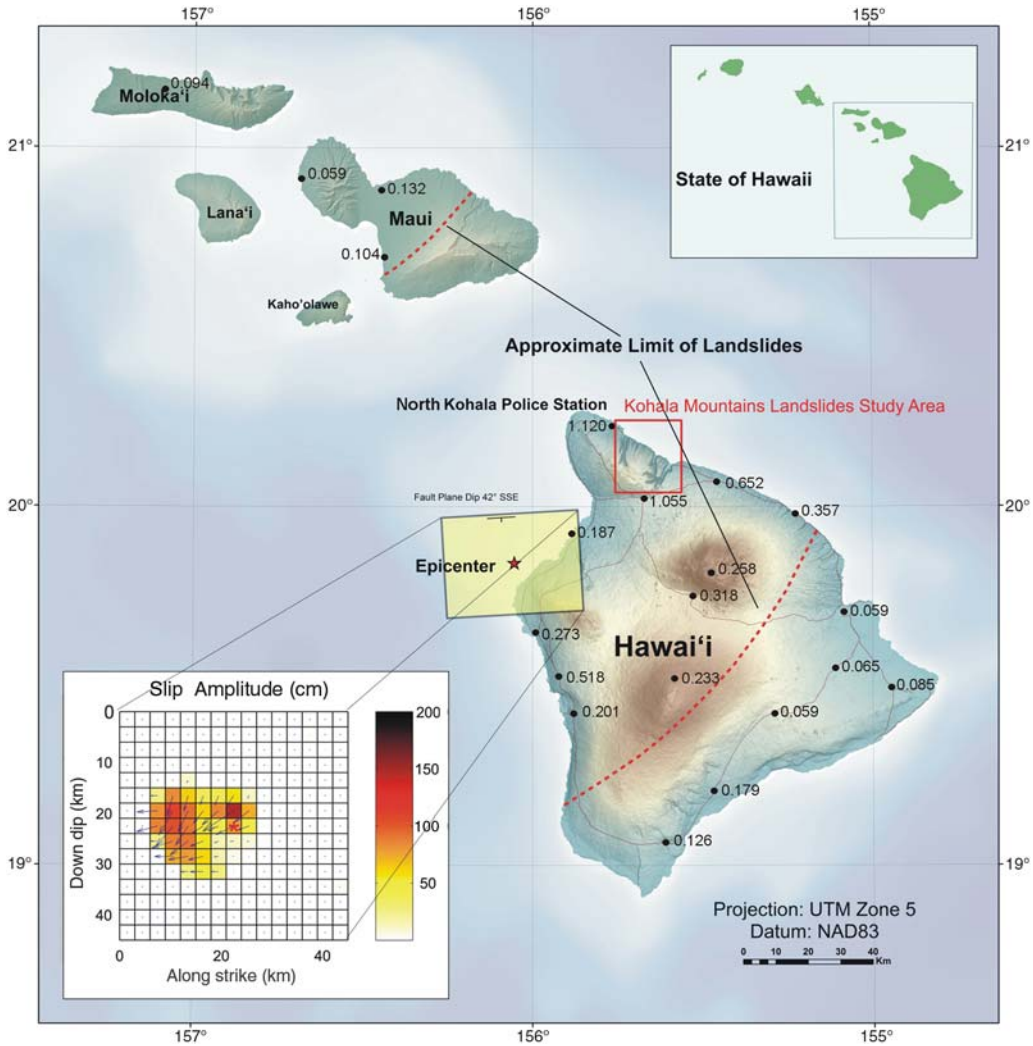

Figure 1. Location map showing the earthquake epicenter, fault-slip model, the Kohala Mountains study area, peak ground accelerations from strong-motion stations recording the earthquake (black dots), and limits of landslides triggered by the earthquake.

Figure 2. Typical small rock falls along the highway on the island of Hawaii, triggered by the Kiholo Bay earthquake.

Figure 3. View from a helicopter of coalescing rock slides on the steep slopes of the Kohala Mountains.

Figure 4. Largest of the rock slides triggered by the Kiholo Bay earthquake. The volume is approximately 10,000 m^3. Location shown in Figure 5a.

at 19.84° N, −156.06° W. Slip is concentrated in a 20 km long horizontal asperity at depths of 40–50 km with a moment magnitude of 6.7. The rendering of topography is based on a 1/3 arc second (10 m) DEM from the U.S. Geological Survey. Topography was approximated in the finite-element grid using a staircase-free surface (Pitarka and Irikura, 1996; Furumura *et al.*, 2003) having 10 grid elements per wavelength to avoid inaccuracies in the linear elements. The region of the finite-element grid, including the earthquake source volume and the Kohala Peninsula, is 90 km long, 56.25 km wide, and 67.5 km deep.

The *P*-wave velocities for our 3D model came from the linear gradient model of Klein (1981), which was developed for routine location of earthquakes on the island of Hawaii. *S*-wave velocities were obtained from the *P*-wave values assuming a Poisson solid. Table 2 gives values from this velocity model at inflections in the velocity gradients. To increase the stability of the calculation, the water layer was excluded and filled with a superficial medium having the same seismic properties as land. The finite-element implementation introduced attenuation by Rayleigh damping. Q-values were based on the shear-wave velocity (V_S) from the formulation by Hartzell *et al.* (2006). Although this model was not developed specifically for Hawaii, there should not be a strong dependence on the model Q-values because of the high surface V_S of 1.1 km/s. On the cliff faces of the Kohala canyons, there is little opportunity for accumulation of sedimentary deposits; and, as such, surface velocities are expected to quickly reach our model velocities.

Figure 6 shows the vector sum of the peak horizontal velocity $(V_x + V_y^2)^{1/2}$ in the Kohala Mountains calculated to a maximum frequency (f) of 3 Hz. The figure shows good correlation of high peak velocity with major slope convexities such as ridge crest and promontories. This simulation uses a node spacing or element length of 43.9 m. Several strong-motion stations on the island of Hawaii recorded the mainshock (Yamada *et al.*, 2010). One station of particular value to this study is located within our modeled region on the northern end of the Kohala Peninsula at the North Kohala Police Station (Fig. 1). Figure 7 compares observed and simulated velocity records at this station. These records have been low-pass filtered at 2 Hz even though the simulation is good to 3 Hz because the Chen Ji teleseismically derived source model has limited high-frequency resolution. As a result, the source does not radiate significant energy above 2 Hz. There is good agreement between the *S*–*P* times and the general character of the waveforms. The higher amplitude of the observations is attributed to lower rigidity sediments at the North Kohala Police Station that are not in our 3D velocity model. We can estimate the effect of these sediments using the shallow shear-wave velocity profile available for this location (Wong *et al.*, 2011) and given in Table 1. Figure 8 shows the *SH* response for this velocity profile with a Q_S of 100 for all layers. Over a broad frequency band, the average amplification is a factor of 2. In the frequency range of our simulation (below 2 Hz), the amplification is approximately a linear function of frequency from a factor of 1.0 to 2.25. These factors are within the range to explain the difference between observed and calculated peak velocities in Figure 7.

We can use the relation of Geli *et al.* (1988), in which a topographic shape ratio of slope height to slope width (h/l) experiences maximum amplification for waves of a similar length given by V_S/f, to estimate where the greatest amplification should occur in the Kohala Mountains. From Figure 7, the dominant frequencies in the ground motion are from 1 to 2 Hz for the 3 Hz simulation. Therefore, topographic features having widths from 550 to 1100 m should experience the greatest excitation. Figure 6 shows this result to be the case. The crests of the broader ridges are the sites of greatest relative amplification, which reaches about a factor of 10 over the lowest calculated ground motion in the study region. The critical width in these considerations is the total width of the topographic feature, not just the width of the top section experiencing the maximum ground motion. By similar reasoning, the cliff faces next to the ocean are also sites of large ground motion. The peak values in Figure 6 can be compared with the vector sum of the horizontal ground velocity from the North Kohala Police Station record. This record yields 20 cm/s low-pass filtered to 2 Hz. Thus, the maximum ground motion from topographic amplification at these frequencies is similar to the ground motion with sediment amplification calculated for the North Kohala Police Station.

Another important effect of topography in addition to amplification of ground motion is extended duration of ground motion from the large number of scattered waves (Bard, 1982; Ma *et al.*, 2007). Figure 9 again plots the vector sum of the horizontal ground velocity for a snapshot in time 28 s after the origin time. At this time, all significant direct arrivals from the source have passed through the study region. The circular pattern of radiated energy consists of scattered waves from the ridge-and-canyon structure of the Kohala Mountains. The wavelength of the scattered waves is controlled by the horizontal scale of the topographic features. These waves also

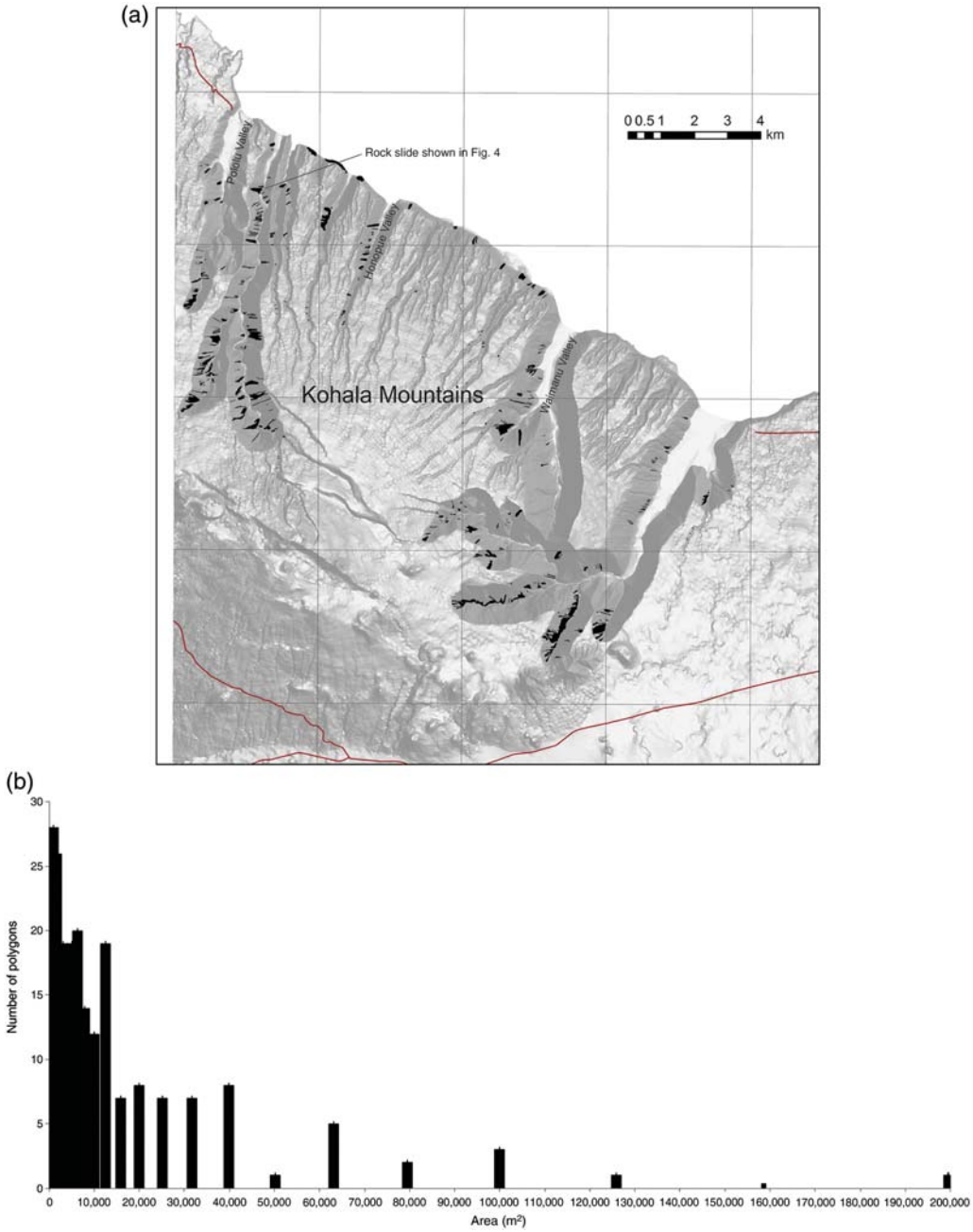

Figure 5. (a) Kohala Mountains study area showing landslides triggered by the Kiholo Bay earthquake (black). (b) The number of landslide polygons in the landslide inventory versus polygon area.

persist at nontrivial levels similar to those shown in Figure 9 for 10 additional seconds. Duration of ground motion has been shown to be an important factor in landslide generation (e.g., Updike *et al.*, 1988; Jibson and Michael, 2009).

To estimate the effect of higher frequency ground motion on the landslide distribution, a 5 Hz simulation was performed using the same source model as the 3 Hz simulation but with substituted source slip time functions that radiate higher frequencies. A Brune (1970, 1971) source time function having a flat displacement spectrum to a corner frequency of 5 Hz was applied to each subfault of the teleseismic source model. This simple approximation might overestimate the high-frequency radiation because the same function was applied regardless of the final slip on the subfault. We make no claim that this is the true source time function for the Kiholo Bay earthquake; it is used simply as an expediency to propagate higher frequencies through the grid because we lack a high-frequency source inversion. The node spacing for this simulation was reduced to 21.9 m. Figure 10 shows the vector sum of the peak horizontal velocities for the 5 Hz simulation. The peak values are not unreasonable considering the maximum of this same measure of ground

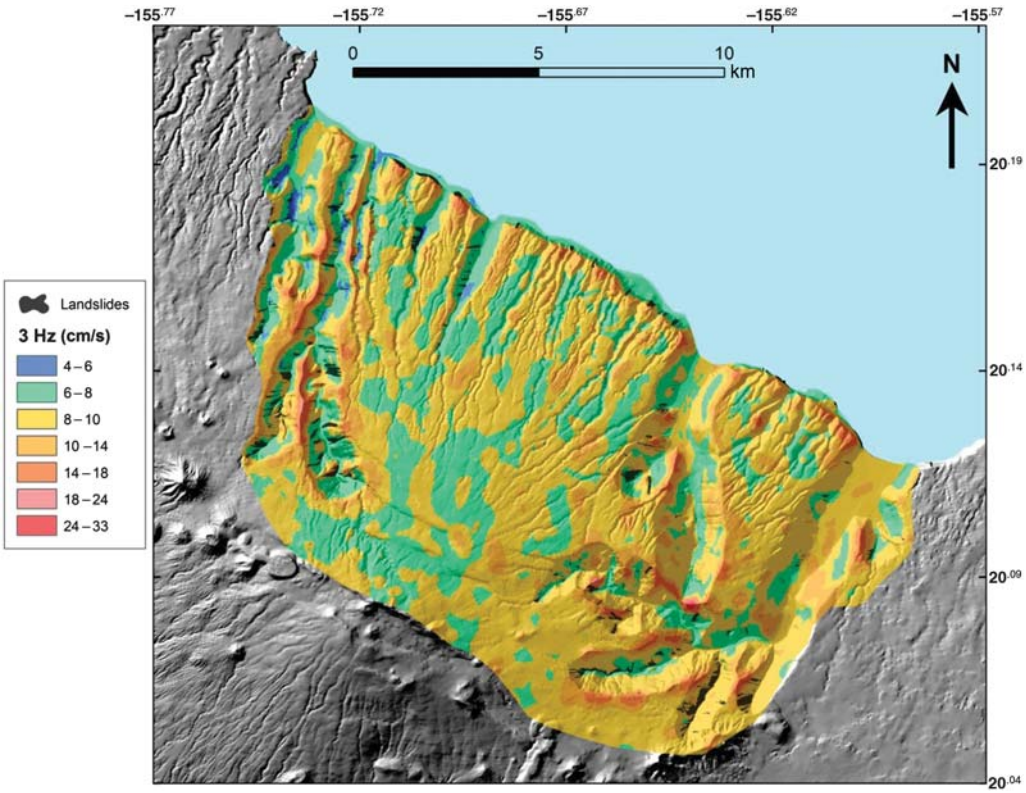

Figure 6. The Kohala Mountains study area showing the vector sum of peak horizontal velocities from the finite-element simulation for frequencies up to 3 Hz.

motion for the North Kohala Police Station record was 40 cm/s when low-pass filtered to 5 Hz. The spatial area that reaches a value of >90 cm/s is small.

Most of the areas that experienced peak ground motions in the 3 Hz simulation also were sites of high ground motion in the 5 Hz simulation. However, in the 5 Hz model the narrower ridge tops also are strongly excited, consistent with the higher frequencies in the input signal. In addition, the areas of strong motion have migrated down into the canyons following secondary convex topographic features along the canyon walls and in the canyon bottoms. This complex pattern of ground motion leads to large differential motions along the canyon walls. Other secondary highs in ground motion in Figure 10 were undoubtedly caused by the constructive interference of scattered waves from adjacent topographic features.

Table 1
Shallow Shear-Wave Velocity at the North Kohala Police Station

Layer	V_S (km/s)	ρ (g/cc)	Thickness (km)
1	0.20	2.1	0.004
2	0.25	2.1	0.008
3	0.40	2.1	0.016
4	0.55	2.2	0.026
5	0.75	2.2	0.034
6	0.90	2.3	0.050
7	1.10	2.3	—

We also considered other measures of ground motion. We plotted duration of ground velocity exceeding a given threshold value and a measure of the cumulative kinetic energy obtained by integrating the square of the ground velocity from both horizontal components. We also calculated ground acceleration at the 3 and 5 Hz limiting frequencies for comparison. The distribution of maxima and minima using these alternative measures is very similar to the velocity plots we show. None of our simulations indicated systematically higher peak velocities on the west sides of canyons as opposed to east sides of canyons. In addition to the measures of ground motion mentioned above, we also simulated surface dynamic shear strain based on the 5 Hz model (Fig. 11) to see if this parameter would capture the large differential motions along the canyon walls generated by the complex ground motions in this canyon topography and compare more favorably with the landslide distribution.

Relation of Modeled Ground Motion to Landslides

Rock falls and rock slides triggered in the canyons of the Kohala Mountains generally were shallow with average thicknesses of less than 2 m. Large slope areas were denuded of vegetation by the coalescence of these falls and slides (Fig. 3). The landslide inventory (Fig. 5a) was compiled by mapping rock falls and rock slides interpreted from color 1:18,000-scale aerial photographs onto 1:25,000-scale

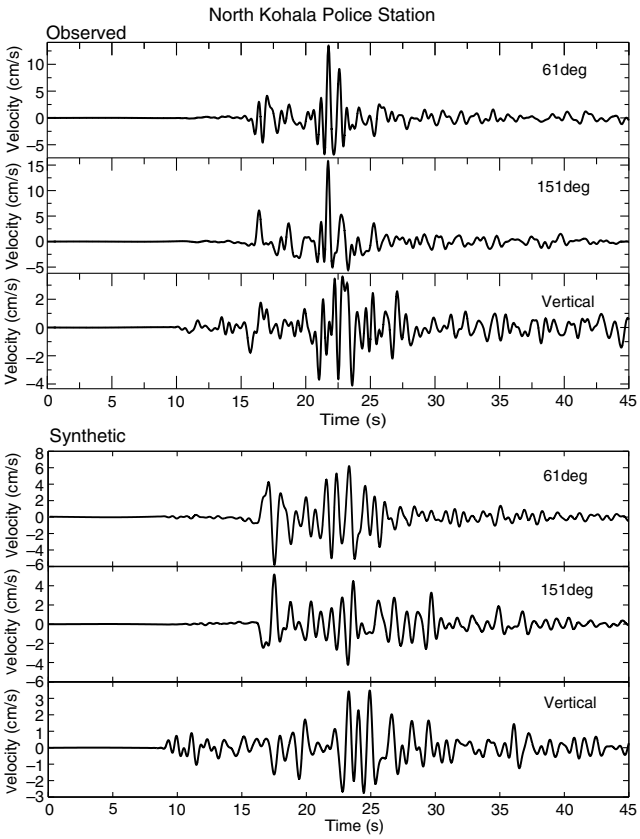

Figure 7. Comparison of observed seismograms and synthetic seismograms from the model simulation at the North Kohala Police Station. Both sets of records are low-pass filtered to 2 Hz.

topographic maps as polygons. The polygons then were digitized and converted to shape files for use in Arc Map 9.3 (size distribution of polygons is shown in Fig. 5b). The area mapped was restricted to the Kohala Mountains (see Fig. 1).

Figures 6 and 10 show the locations of the mapped rock falls and rock slides with respect to the peak velocities in each cell of the DEM for two simulations, 3 and 5 Hz, respectively. The ranges of velocities in the 3 Hz simulation are much lower than those from the 5 Hz simulation; therefore, the values of the colors of the various velocity categories differ between the 3 and 5 Hz simulations in Figures 6 and 10. Figure 6 shows that, although some landslide locations correlate with high-velocity zones, no systematic correlation between landslide locations and high peak velocities is apparent. Maximum velocities occur consistently on the most prominent ridge crests, whereas the landslide population is more randomly distributed on ridge crests and flanks. The location of maximum peak velocities on ridge crests and promontories is similar to where landslides have been observed in other earthquakes (Harp and Jibson, 1995, 1996; Meunier *et al.*, 2008). Rock falls and slides triggered by the Kiholo Bay earthquake, however, have no similar clustering with respect to slope elevation. The limitation of the simulation shown in Figure 6 to frequencies no higher than 3 Hz is somewhat problematic because shallow rock falls and rock slides are commonly believed to be triggered by shaking frequencies as high as 10 Hz (Jibson *et al.*, 2004). Figure 10 shows high peak velocities associated not only with major ridge tops and promontories, but also with numerous minor convexities near the tops of ridges, along canyon walls, and at canyon bottoms. This simulation, including frequencies up to 5 Hz, shows more areas of high peak velocities and has better correlation with landslide locations than Figure 6. However, the collocations of high velocities and landslides are still relatively poor, and many landslides are located in areas of low velocity. Neither simulation shows an asymmetric pattern of ground motion with higher peak velocities on east-facing canyon slopes than west-facing slopes.

A visual comparison of the landslide distribution with surface dynamic shear strain (Fig. 11) shows a significantly better correlation than with peak velocities. The highest values of dynamic strain (in microstrain, 1×10^{-6}) occur within the steep canyons of the Kohala Mountains where the landslides are located. Low values of strain conversely are found above the canyons on the plateau-like surface be-

Table 2
Velocity Gradient Model Used in Finite-Element Simulations

Inflection Point	V_P (km/s)	V_S (km/s)	ρ (g/cc)	Depth (km)
1	1.9	1.10	2.0	0.
2	6.5	3.75	2.8	4.6
3	6.9	3.98	3.0	15.0
4	8.3	4.50	3.3	16.5
5	8.3	4.50	3.3	68.0

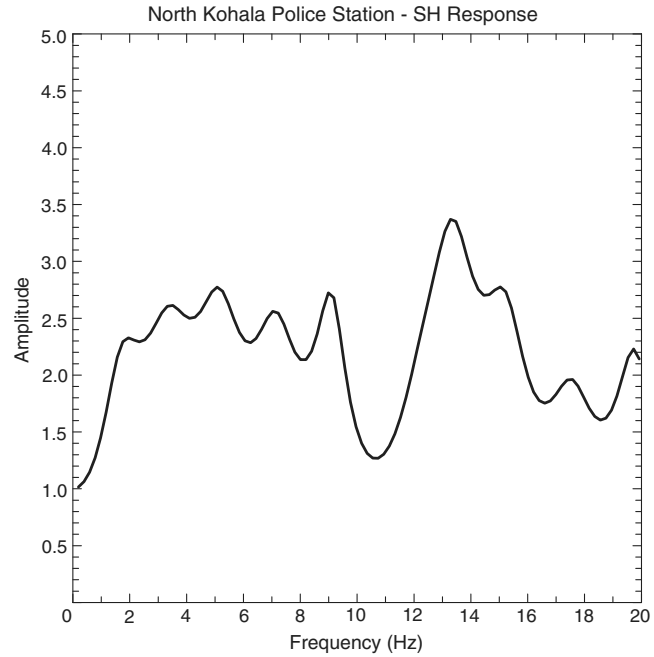

Figure 8. *SH* response for the shallow velocity profile at the North Kohala Police Station.

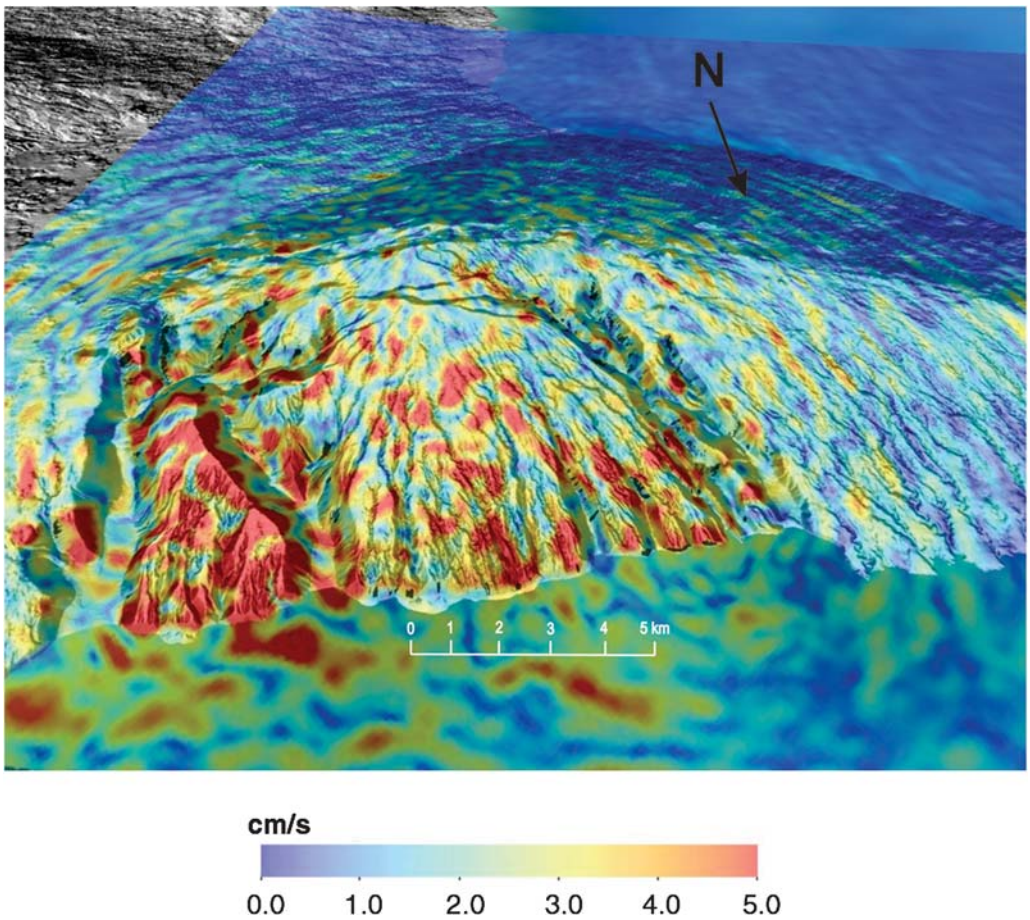

Figure 9. Oblique southward view of the Kohala Mountains study area showing the vector sum of peak horizontal velocities at a time slice of 28 s after the origin time from the 3 Hz finite-element simulation. Circular patterns show radiated energy after passage of most of the seismic waves from the source.

tween the canyon margins. It therefore seems at first glance that dynamic shear strain correlates better with locations of seismically triggered landslides than does peak velocity. The following section is a quantitative comparison of the respective velocity and strain simulations with the locations of the landslide polygons. For this comparison, only the upper portions (the landslide source areas) of the landslide polygons were considered.

Statistical Evaluation of the Predictions

We used a "ratio of effectiveness" (Chung and Fabbri, 2003) to quantify the success of different velocity levels in the 3 and 5 Hz simulations in predicting the landslide locations. This ratio, R_v, is defined as the concentration of landslide cells within a velocity category in percent (i.e., all cells within this range of velocities that are from the source areas of landslide polygons), divided by the concentration of landslide cells within the entire study area in percent R_{Total}. The ratio R_v/R_{Total} is a measure of the effectiveness of the velocity category in predicting landslide spatial density compared to the landslide spatial density of the entire area. Chung and Fabbri (2003) stated that ratios of 3.0 or greater are significant positive predictors, and ratios of 0.2 or less are significant negative predictors. Figure 12 shows a histogram of these ratios for the 3 and 5 Hz simulations. The velocity categories for each simulation were selected at regular logarithmic spacings of the total ranges of velocity data.

For the 3 Hz simulation (Fig. 12a), only the highest velocity category, >18 cm/s is a significant predictor ($R_v/R_{Total} = 10.46$) of landslide locations. All of the lower velocity categories are below the ratio value of 3.0 that indicates good prediction. For the 5 Hz simulation (Fig. 12b), the two uppermost categories, 42–64 cm/s and >64 cm/s are significant predictors with ratios of 6.56 and 14.02, respectively. Again, the lower velocity categories are poor predictors with ratio values less than 3.0. The highest velocity categories in both the 3 and 5 Hz simulations, however, are less statistically robust than the other categories because they contain relatively little data.

Evaluation of the predictive effectiveness of dynamic shear strain (Fig. 12c) indicates that most of the higher categories of strain are good predictors; results show an almost monotonic increase in predictive values with increasing strain. Categories of strain levels beginning with 121–163

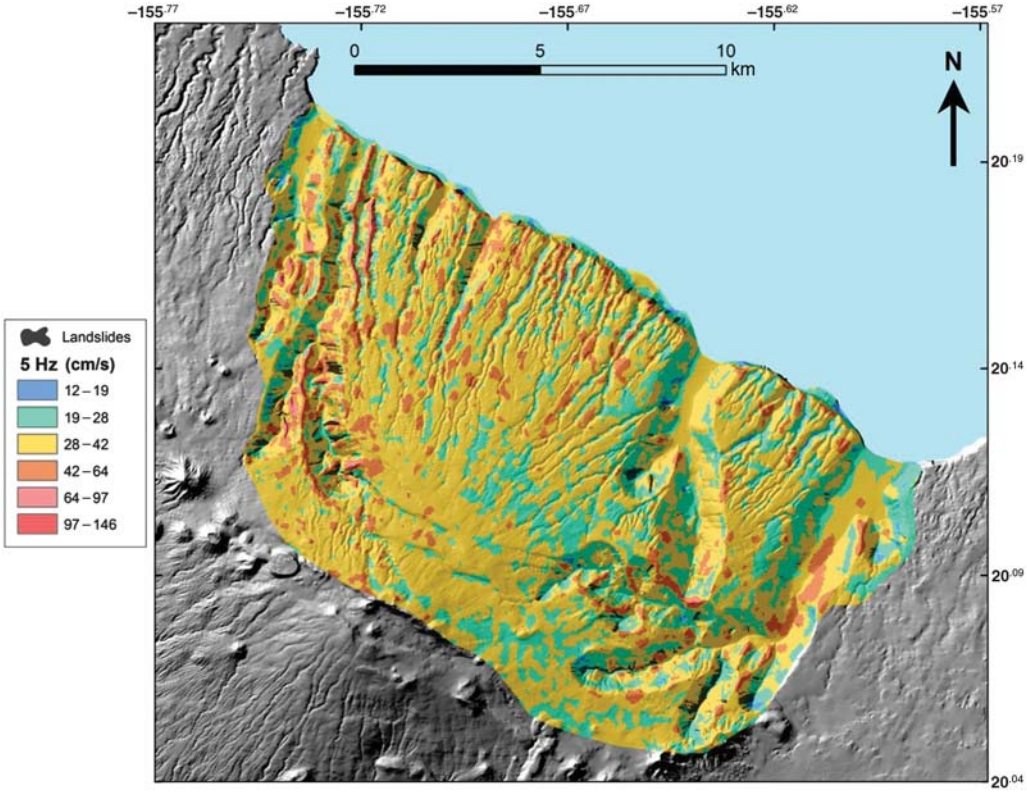

Figure 10. The Kohala Mountains study area showing the vector sum of the peak horizontal velocities from finite-element simulation for frequencies up to 5 Hz.

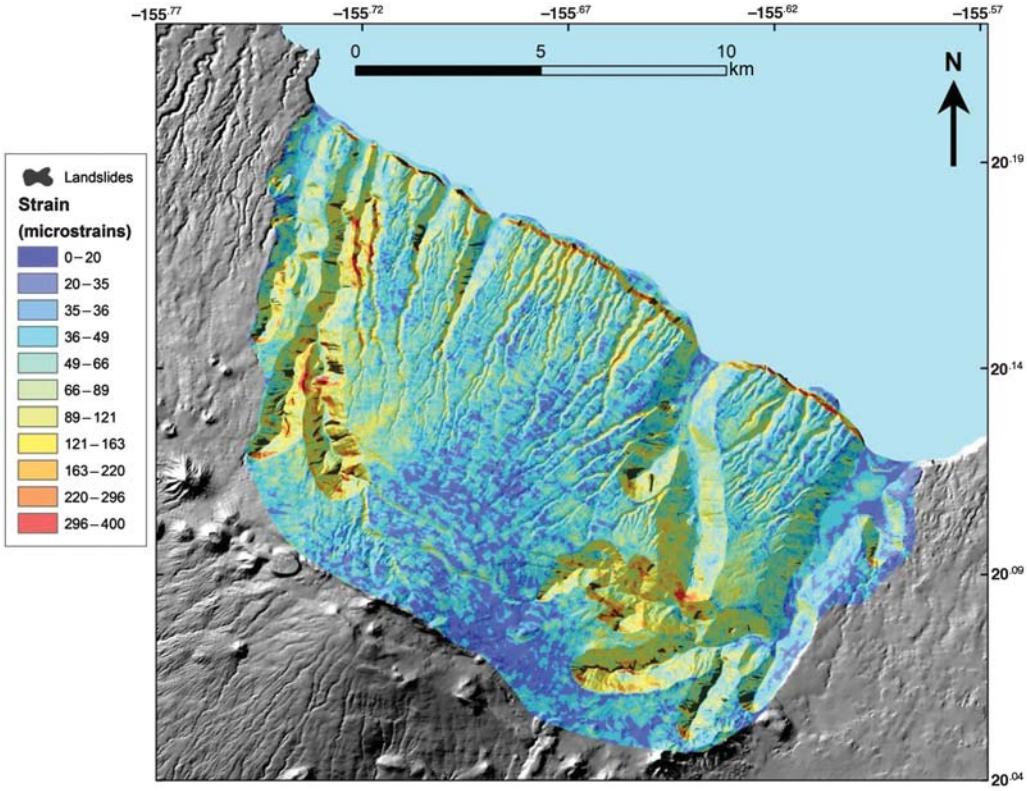

Figure 11. The Kohala Mountains study area showing surface dynamic shear strain (microstrains, 1×10^{-6}) from the 5 Hz simulation.

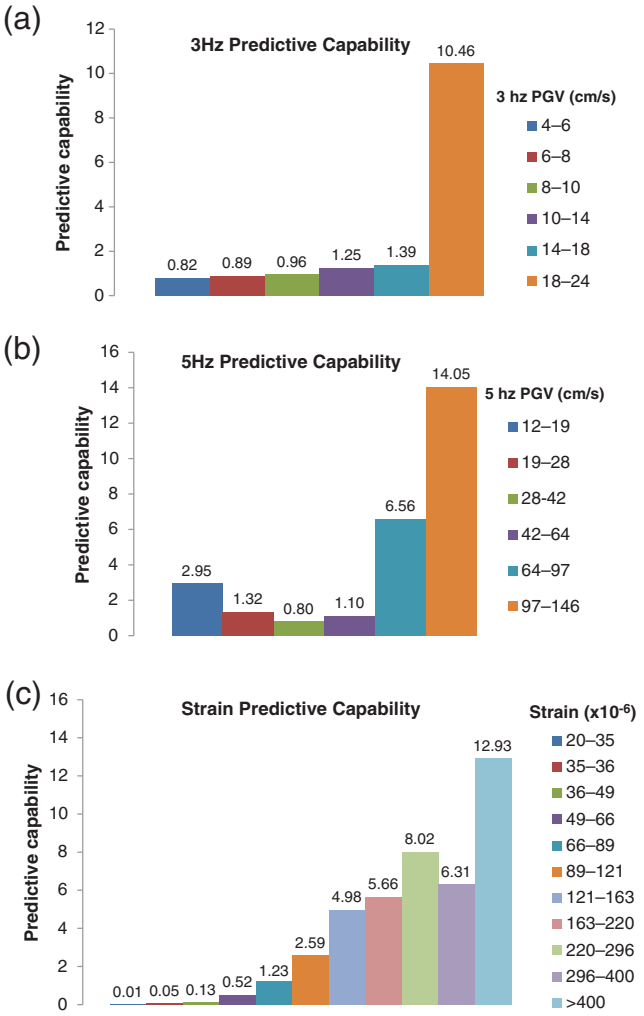

Figure 12. Predictive capabilities for (a) peak velocity up to 3 Hz, (b) peak velocity up to 5 Hz, and (c) dynamic shear strain.

microstrains ($R_s/R_{\text{Total}} = 4.98$) increase in ratio values to >400 microstrains ($R_s/R_{\text{Total}} = 12.93$), with the exception of the 296–400 microstrains category, ($R_s/R_{\text{Total}} = 6.31$). The fact that the upper five strain categories have significant predictive ratios and that the ratios generally increase with increasing strain values indicates that the dynamic shear strain pattern in Figure 11 is a much better predictor of landslide locations triggered by this earthquake than either of the peak-velocity distributions.

Discussion

The collocation of high peak velocities with ridge crests and other slope convexities in Figures 6 and 10 demonstrates the facility of the strong-motion velocity model in predicting the kinds of topographic amplification that we have observed in many earthquakes, as evidenced by landslide distributions and deformation of ridge crests (Harp *et al.*, 1981; Harp and Jibson, 1996; Jibson *et al.*, 2004). The landslide distribution within the Kohala Mountains triggered by the 2006 earthquake, however, does not exhibit such a pronounced correlation with ridge crests and other topographic convexities. The juxtaposition of earthquake-triggered landslides and peak-velocity values shown in Figures 6 and 10 shows close collocations in some areas (more so in Fig. 10), but many other areas show poor spatial correlation as quantified in Figure 12a,b. Several possible reasons might explain this.

The first possibility is that spatial variation in ground motion (as measured by peak velocity) does not directly produce the landslide distribution. The distribution of landslides could be controlled more by local variations in landslide susceptibility due to variations in material properties of the slope-forming soil and weathered bedrock. This appears not to be the case, however. The slope-forming materials (alternating basalt flows and breccias) present on all canyon slopes appear similar. The bedding approaches horizontal so there is little difference in the orientation of discontinuities with respect to slope aspect that would create a significant susceptibility difference at different locations. If slopes of different aspects received more moisture as a result of the prevailing wind direction, then weathering and its attendant effects on susceptibility of slopes might vary with slope orientation. Although the prevailing wind direction is from east to west due to trade-wind flow, winds are turbulent within the canyons so there are few slopes protected from the wind. Soil thickness appears to be very similar on all slopes regardless of aspect or vertical position on the slope. The steepness of the slopes in the Kohala Mountains varies consistently from about 60° to 80°. This range of steepness is relatively invariant regardless of aspect or location in the canyons whether at the heads of canyons or at their mouths at the coast. Thus, in the absence of susceptibility differences, variation in ground shaking or deformation appears to be the logical cause of the landslide distribution.

The second possible reason for the failure of the ground-motion model to consistently predict landslide locations is that the model, despite its sophistication, remains deficient in some areas that pertain to landslide triggering. One significant issue is that the frequency range of the ground-motion model extends only as high as 3 Hz in the simulation shown in Figure 6 and 5 Hz in Figure 10. Shallow, brittle rock falls and rock slides such as those that occurred in the Kohala Mountains could be triggered by higher frequency shaking up to 10 Hz or even 20 Hz, as indicated by unpublished data from aftershocks in other earthquakes (E. L. Harp, 1983, unpublished data). Modeling frequencies in this range is prohibitive, however, because of the huge model sizes that would be required.

The shear-wave velocity model used (Klein, 1981) and the assumption of an approximate Poisson solid might not faithfully replicate the velocities of the shallowest layers in the Kohala Mountains. The Klein (1981) velocity model has been used to locate earthquakes and has minimum V_S of 1100 m/s for the surface materials, which might not be appropriate at the surface due to the presence of a thin weathered layer. Most of the triggered landslides would have oc-

curred in this surficial layer that could have a much lower V_S value.

Another complicating factor is that comparing precisely located landslides with a ground-motion model derived from teleseismic records that do not include the full spectrum of frequencies felt by the slopes from the mainshock yields only a limited resolution of ground-motion variability.

These limitations of the frequency range, shear-wave velocity model, and resolution could significantly affect the simulated interaction of shear-wave frequencies with the spatial wavelengths of the canyon topography. For example, the frequency limit of 5 Hz results in a resampling of the 10 m DEM to a minimum grid spacing of 21.9 m. This resampling of topography might not be fine enough to capture the features responsible for the initiation of landslides.

Finally, as mentioned above, large differential motions occur on the slopes of topographic features as a result of the interference between incoming waves and outgoing diffracted waves (Bard, 1982; Geli *et al.*, 1988). These possible interference effects and the presence of significant velocity gradients shown in Figures 6 and 10 led us to investigate the possible effects of dynamic shear strain as a cause of the landslide distribution.

The results shown in Figure 12 indicating the predictive capability of dynamic shear strain suggest that, instead of a threshold level of shear strain above which correlation with landslides is relatively constant, the ratio of effectiveness increases steadily from the middle levels of strain to the highest and that increasing levels of strain lead to higher correlation with landslides. Whether this effect might be due to small variations of susceptibility from place to place on the canyon slopes or simply to strain levels is not clear.

Dynamic strain imposed by the earthquake shaking is a direct measure of the deformation of the slope surface. The cyclical variation in shear stress and strain within the surficial volcanic soil and weathered bedrock could be a causative factor in the decoupling of landslide material from underlying slopes. Inertial shaking forces as measured by acceleration or velocity have traditionally been considered as the logical causes of seismic landslide initiation, but our results suggest the vibrational strain that occurs during earthquake shaking within surficial materials could actually be the more important parameter leading to slope failure. This possibility needs further investigation to see if similar correlations between dynamic shear strain and landslide distributions exist in other earthquakes.

Conclusions

The comparison of peak ground-motion values (vector sum of two orthogonal horizontal components of velocity) and landslides triggered by the Kiholo Bay earthquake in the Kohala Mountains of the island of Hawaii indicates mixed results. Some landslide locations are well correlated with high peak velocities, but many are not. The most likely reasons for this lack of consistent spatial correlation with peak velocities are (1) an upper-bound frequency limit of 3–5 Hz in modeling the strong ground motion, which is possibly lower than the triggering frequency range for shallow landslides; (2) the assumption of a minimum shear-wave velocity at the surface of 1100 m/s, which is likely higher than the shear-wave velocity in the surficial weathered zone that produced the landslides; and (3) smoothing of the topography by resampling the 10 m DEM during the simulations.

Comparison of the landslide distribution with dynamic shear strain produces distinctly improved results, shown quantitatively in Figure 12. Significant correlation of dynamic strain with landslide distributions has not been previously attempted or even considered. The fact that the simulated strain field closely matches the areas of landslide incidence suggests that similar comparisons need to be conducted on landslide distributions triggered by other earthquakes.

This study represents the first attempt to match ground motion from a 3D velocity model and finite-element simulations to a detailed landslide inventory. The results probably could be improved by including higher frequency information from the local strong-motion records in the source model. Also, a more accurate shear-wave velocity model calibrated to the local stratigraphic section would likely improve the results. We did not attempt to do this at this time for practical limitations of file sizes and computer-analysis time. The current model, however, demonstrates the possibilities of using 3D ground-motion modeling to predict the spatial distribution of seismically triggered landslides.

Data and Resources

Earthquake magnitudes are from http://earthquake.usgs.gov/earthquakes (last accessed February 2014). The North Kohala Police Station record is from Chris Stevens, U.S. Geological Survey (USGS) unpublished data. The elevation data used here are derived using the 1/3 arc second USGS Digital Elevation Model of the region, available at http://nationalmap.gov/viewer.html (last accessed February 2014).

Acknowledgments

We thank Chris Stevens of the U.S. Geological Survey for supplying the digitized analog files from the North Kohala Police Station for our use.

References

Bard, P.-Y. (1982). Diffracted waves and displacement field over two-dimensional elevated topographies, *Geophys. J. Roy. Astron. Soc.* **71,** 731–760.

Bielak, J., R. W. Graves, K. B. Olsen, R. Taborda, L. Ramírez-Guzmán, S. M. Day, G. P. Ely, D. Roten, T. H. Jordan, P. J. Maechling, and G. Juve (2010). The ShakeOut earthquake scenario: Verification of three simulation sets, *Geophys. J. Int.* **180,** 375–404.

Bouchon, M. (1973). Effect of topography on surface motion, *Bull. Seismol. Soc. Am.* **63,** 615–632.

Brune, J. N. (1970). Tectonic stress and spectra of seismic shear waves from earthquakes, *J. Geophys. Res.* **75,** 4997–5009.

Brune, J. N. (1971). Correction, *J. Geophys. Res.* **76,** 5002.

Çelebi, M. (Editor) (1986). Seismic site-response experiments following the March 3, 1985 central Chile earthquake (topographical and geological effects), *U.S. Geol. Surv. Open-File Rept. 86-90*, 206 pp.

Chung, C. F., and A. G. Fabbri (2003). Validation of spatial prediction models for landslide hazard mapping, *Nat. Hazards* **30,** 451–472.

Dai, F. C., C. Xu, X. Yao, L. Xu, X. B. Tu, and Q. M. Gong (2011). Spatial distribution of landslides triggered by the 2008 M_s 8.0 Wenchuan earthquake, China, *J. Asian Earth Sci.* **40,** 883–895.

Furumura, T., B. L. N. Kennett, and K. Koketsu (2003). Visualization of 3D wave propagation from the 2000 Tottori-ken Seibu, Japan, earthquake: Observation and numerical simulation, *Bull. Seismol. Soc. Am.* **93,** 870–881.

Geli, L., P.-Y. Bard, and B. Jullien (1988). The effect of topography on earthquake ground motion: A review and new results, *Bull. Seismol. Soc. Am.* **78,** 42–63.

Harp, E. L., and R. W. Jibson (1995). Inventory of landslides triggered by the 1994 Northridge, California earthquake, *U.S. Geol. Surv. Open-File Rept. 95-213*, 17 pp.

Harp, E. L., and R. W. Jibson (1996). Landslides triggered by the 1994 Northridge, California, earthquake, *Bull. Seismol. Soc. Am.* **86,** no. 1B, S319–S332.

Harp, E. L., and R. W. Jibson (2002). Anomalous concentrations of seismically triggered rock falls in Pacoima Canyon: Are they caused by highly susceptible slopes or local amplification of seismic shaking? *Bull. Seismol. Soc. Am.* **92,** 3180–3189.

Harp, E. L., and R. W. Jibson (2007). Landslides triggered by the M 6.7 October 15, 2006, Kiholo Bay earthquake, Hawaii, *Seismol. Res. Lett.* **78,** 297.

Harp, E. L., and R. C. Wilson (1995). Shaking intensity thresholds for rock falls and slides: Evidence from the 1987 Whittier Narrows and Superstition Hills earthquake strong-motion records, *Bull. Seismol. Soc. Am.* **85,** 1739–1757.

Harp, E. L., R. W. Jibson, and Y. Zeng (2008). Spatial inventory of landslides triggered by the M 6.7 October 15, 2006, Kiholo Bay earthquake, Hawaii, *Seismol. Res. Lett.* **79,** 278.

Harp, E. L., R. C. Wilson, and G. F. Wieczorek (1981). Landslides from the February 4, 1976, Guatemala earthquake, *U.S. Geol. Surv. Prof. Pap. 1204A*, 35 pp.

Hartzell, S. H., D. L. Carver, and K. W. King (1994). Initial investigation of site and topographic effects at Robinwood Ridge, California, *Bull. Seismol. Soc. Am.* **84,** 1336–1349.

Hartzell, S., S. Harmsen, R. A. Williams, D. Carver, A. Frankel, G. Choy, P.-C. Liu, R. C. Jachens, T. M. Brocher, and C. M. Wentworth (2006). Modeling and validation of a 3D velocity structure for the Santa Clara Valley, California, for seismic-wave simulations, *Bull. Seismol. Soc. Am.* **96,** 1851–1881.

Hartzell, S., M. Meremonte, L. Ramirez-Guzman, and D. McNamara (2014). Ground motion in the presence of complex topography: Earthquake and ambient noise sources, *Bull. Seismol. Soc. Am.* **104,** 451–466.

Jibson, R. W., and E. L. Harp (2012). Extraordinary distance limits of landslide triggered by the 2011 Mineral, Virginia, earthquake, *Bull. Seismol. Soc. Am.* **102,** 2368–2377.

Jibson, R. W., and J. A. Michael (2009). Maps showing seismic landslide hazards in Anchorage, Alaska, *U.S. Geol. Surv. Scientific Investigations Map 3077*, 2 pl., 11 pp. (pamphlet).

Jibson, R. W., E. L. Harp, and J. A. Michael (2000). A method for producing digital probabilistic seismic landslide hazard maps, *Eng. Geol.* **58,** 271–289.

Jibson, R. W., E. L. Harp, W. Schulz, and D. K. Keefer (2004). Landslides triggered by the 2002 Denali Fault, Alaska, earthquake and the inferred nature of strong shaking, *Earthq. Spectra* **20,** 669–691.

Khazai, B., and N. Sitar (2003). Evaluation of factors controlling earthquake-induced landslides caused by Chi-Chi earthquake and comparison with the Northridge and Loma Prieta events, *Eng. Geol.* **71,** 79–95.

Klein, F. W. (1981). A linear gradient crustal model for south Hawaii, *Bull. Seismol. Soc. Am.* **71,** 1503–1510.

Lee, C.-T., C.-C. Huang, J.-F. Lee, K.-L. Pan, M.-L. Lin, and J.-J. Dong (2008). Statistical approach to earthquake-induced landslide susceptibility, *Eng. Geol.* **100,** 43–58.

Lee, S.-J., Y.-C. Chan, D. Komatitsch, B.-S. Huang, and J. Tromp (2009). Effects of realistic surface topography on seismic ground motion in the Yangminshan region of Taiwan based upon the spectral-element method and LiDAR DTM, *Bull. Seismol. Soc. Am.* **99,** 681–693.

Lin, M.-L., and C.-C. Tung (2003). A GIS-based potential analysis of the landslides induced by the Chi-Chi earthquake, *Eng. Geol.* **71,** 63–77.

Ma, S., R. J. Archuleta, and M. T. Page (2007). Effects of large-scale surface topography on ground motions, as demonstrated by a study of the San Gabriel Mountains, Los Angeles, California, *Bull. Seismol. Soc. Am.* **97,** 2066–2079.

Meunier, P., N. Hovius, and J. A. Haines (2007). Regional patterns of earthquake-triggered landslides and their relation to ground motion, *Geophys. Res. Lett.* **34,** L20408, doi: 10.1029/2007GL031337.

Meunier, P., N. Hovius, and J. A. Haines (2008). Topographic site effects and the location of earthquake induced landslides, *Earth Planet. Sci. Lett.* **275,** 221–232, doi: 10.1016/j.epsl.2008.07.020.

Pitarka, A., and K. Irikura (1996). Basin structure effects on long-period strong motions in the San Fernando Valley and the Los Angeles Basin from the 1994 Northridge earthquake and an aftershock, *Bull. Seismol. Soc. Am.* **86,** no. 1B, S126–S137.

Sepulveda, S. A., W. Murphy, R. W. Jibson, and D. N. Petley (2005). Seismically induced rock slope failures resulting from topographic amplification of strong ground motions: The case of Pacoima Canyon, California, *Eng. Geol.* **80,** 336–348.

Tu, T., H. Yu, L. Ramírez-Guzmán, J. Bielak, O. Ghattas, K. L. Ma, and D. O'Halloran (2006). From mesh generation to parallel supercomputing, in *Proceedings of the 2006 ACM/IEEE Conference on Supercomputing*, Tampa, Florida.

Updike, R. G., J. A. Egan, Y. Moriwaki, I. M. Idriss, and T. L. Moses (1988). A model for earthquake-induced translatory landslides in Quaternary sediments, *Geol. Soc. Am. Bull.* **100,** 783–792.

Wang, X., G. Nie, and D. Wang (2010). Research on the relationship between landslides and peak ground acceleration induced by Wenchuan earthquake, *Chin. J. Rock Mech. Eng.* **29,** 82–89.

Wong, I. G., K. H. Stokoe II, B. R. Cox, J. Yuan, K. L. Knudsen, F. Terra, P. Okudo, and Y.-C. Lin (2011). Shear-wave velocity characterization of the USGS Hawaiian strong-motion network on the island of Hawaii and development of an NEHRP site-class map, *Bull. Seismol. Soc. Am.* **101,** 2252–2269.

Yamada, T., P. G. Okubo, and C. J. Wolfe (2010). Kiholo Bay, Hawaii, earthquake sequence of 2006: Relationship of the mainshock slip with locations and source parameters of aftershocks, *J. Geophys. Res.* **115,** no. B08304, doi: 10.1029/2009JB006657.

U.S. Geological Survey
1711 Illinois St.
Golden, Colorado 80401
(E.L.H., S.H.H., R.W.J., R.G.S.)

Instituto de Ingenieria Coordinacion de Sismologia e Instrumentacion Sismica
Universidad Nacional Autonoma de Mexico Av. Universidad No. 3000
Coyoacán, Mexico D.F. 04510
(L.R.-G.)

Manuscript received 21 February 2014;
Published Online 16 September 2014